



Efficient ORR catalysts for zinc-air battery: Biomass-derived ultra-stable Co nanoparticles wrapped with graphitic layers via optimizing electron transfer

Yu Feng^a, Kexin Song^a, Wei Zhang^{a,*}, Xinyan Zhou^a, Seung Jo Yoo^b, Jin-Gyu Kim^b, Sifan Qiao^a, Yugang Qi^a, Xu Zou^a, Zhongjun Chen^c, Tingting Qin^a, Nailin Yue^a, Zizhun Wang^a, Dabing Li^d, Weitao Zheng^{a,*}

^aState Key Laboratory of Automotive Simulation and Control, School of Materials Science & Engineering, Key Laboratory of Automobile Materials MOE, Electron Microscopy Center, and International Center of Future Science, Jilin University, Changchun 130012, Jilin, China

^bDivision of Scientific Instrumentation & Management, Korea Basic Science Institute, Daejeon 34133, Republic of Korea

^cInstitute of High Energy Physics, Chinese Academy of Sciences, Beijing 100049, China

^dState Key Laboratory of Luminescence and Applications, Changchun Institute of Optics, Fine Mechanics and Physics, Chinese Academy of Sciences, Changchun 130033, Jilin, China

ARTICLE INFO

Article history:

Received 31 December 2021

Revised 27 January 2022

Accepted 28 January 2022

Available online 5 February 2022

Keywords:

Chainmail catalyst

Graphitic layers

Co nanoparticles

Oxygen reduction reaction

ABSTRACT

The poor stability of non-noble metal catalysts in oxygen reduction reaction (ORR) is a main bottleneck that limits their big-scale application in metal-air batteries. Herein, we construct a chainmail catalyst (Co-NC-AD) with outstanding stability, via the competitive complexation and post absorption strategy, consisting of highly graphitic layers wrapped uniform-size Co nanoparticles (Co-NPs). Experiments combined with density functional theory (DFT) calculations jointly confirmed that the electron transfer occurred from the inner Co-NPs to the external graphitic layers. It facilitated the adsorption process of oxygen molecules and the hybridization of the O-2p and C-1p orbitals, which accelerated the ORR reaction kinetics. Consequently, our prepared Co-NC-AD shows excellent ORR activity, offered with a more positive initial potential ($E_{\text{onset}} = 0.95$ V) and half-wave potential ($E_{1/2} = 0.86$ V). The remarkable stability and resistance of methanol poisoning are merited from the protection effect of stable graphitic layers. In addition, the high electrochemical performance of Co-NC-AD-based zinc-air battery demonstrates their potential for practical applications. Therefore, our work provides new ideas for the design of nano-confined catalysts with high stability and activity.

© 2022 Science Press and Dalian Institute of Chemical Physics, Chinese Academy of Sciences. Published by ELSEVIER B.V. and Science Press. All rights reserved.

1. Introduction

As an important cathode reaction of metal-air batteries and fuel cells, oxygen reduction reaction (ORR) often requires the introduction of electrocatalysts to accelerate the reaction efficiency due to its intrinsic low reaction kinetics. Noble metal catalysts represented by Pt-based metals are widely commercialized due to their superior ORR activities [1–6], however, suffering from low earth abundance and unsatisfying endurance blocking for their large-scale application. Therefore, it is urgent to develop some candidates with low cost and high activity [7–10]. Carbon materials are promising catalytic materials due to the advantages of high conductivity, abundant sources, excellent controllability and sta-

bility, suffering from the poor intrinsic catalytic activity of carbon materials. Thus, doping atoms with a variety of electronegativity and radii enable modifying the surface charge distribution and spin density [11,12]. Nitrogen is the most common doping element due to its similar atomic structure and strong covalent bond to carbon [13–16]. Although the catalytic activity of nitrogen-doped carbon (NC) has been improved in comparison with carbon, a satisfactory catalytic activity remains to be achieved [17–20].

Transition metal-based catalysts hold unfilled 3d-orbitals for higher ORR activity [21–25]. However, active centers usually suffer from a relatively low work function, thereof strong reactivity and susceptibility to phase change in oxidizing or corrosive environments. So, poor stability and easy toxicity cannot be bypassed [26–28]. Recently, Deng and Bao group has proposed the concept of “chainmail catalyst”, in which metal cores are wrapped with stable graphitic layers to avoid a direct contact with those harsh reaction environments, effectively enhancing the long-term cycl-

* Corresponding authors.

E-mail addresses: weizhang@jlu.edu.cn (W. Zhang), wz Zheng@jlu.edu.cn (W. Zheng).

bility [29–32]. Studies have manifested that the different work functions exist between metal nanoparticles (M-NPs) and their outer graphite layers. They manipulate the internal M-NPs cores to transfer electrons to the outer surface of the graphite layers, thereby effectively controlling the charge distribution and spin density on the carbon surface [33–35]. The graphitic layers provide a large amount of active sites, and the moderate adsorption strength between the active sites and intermediate species is conducive to the improvement of catalytic activity [36–38]. Despite these advances, the “chainmail catalyst” still confronts some challenges: how to maximize its catalytic activity by simultaneously guaranteeing its high stability [30]. In addition, expensive nanomaterial precursors and complex synthesis conditions have also brought challenges to the practical application of “chainmail catalyst”. The strategy of preparing carbon-based chainmail catalysts from biomass materials can effectively alleviate these difficulties [39,40]. As a low-cost biomass material, chitosan has a good chelating capability to metal ions due to its abundance of amino and carboxyl groups. The abundant carbon and nitrogen contents make it a suitable precursor for the preparation of carbon-based chainmail catalysts.

In this paper, we used the cheap biomass material-chitosan through secondary pyrolysis and post-adsorption to synthesize a “chainmail catalyst” with high stability and high catalytic activity. The optimized Co-NC-AD (AD presents post adsorption process) showed excellent ORR activity ($E_{1/2} = 0.86$ V, $E_{\text{onset}} = 0.95$ V) comparable to the commercial Pt/C ($E_{1/2} = 0.84$ V, $E_{\text{onset}} = 0.95$ V) and most non-noble metal catalysts in 0.1 M KOH solution, as well as good stability and methanol resistance. Combined with density functional theory (DFT) calculation and spectrum analysis, the excellent ORR activity is mainly derived from that the electron transfer between the inner Co-NPs and the outer graphitic layers, as it leads to the changes in the electron distribution of the graphitic layers, which is conducive to the adsorption between oxygen molecules and active sites. The graphitic layers improved the catalyst stability by avoiding a direct contact between the inner metal core and highly corrosive environment. The zinc-air battery with Co-NC-AD showed high power density (194 mW cm⁻¹) and specific capacity (808 mAh g_{Zn}⁻¹) merited from excellent ORR activity. Our work has positive significance for simple synthesis and performance improvement of “chainmail catalysts”.

2. Experimental

2.1. Synthesis process

2.1.1. Synthesis of NC

Acetic acid (0.6 mL) and chitosan (0.6 g) were dissolved in 20 mL deionized water. The mixture was freeze-dried and transferred to a porcelain boat. The samples were heated in a tube furnace at 5 °C min⁻¹ and kept 900 °C for 2 h to obtain NCs.

2.1.2. Synthesis of Co/NC

Acetic acid (0.6 mL), chitosan (0.6 g), and cobalt acetate tetrahydrate (199.2 mg) were dissolved in 20 mL deionized water. The mixture was freeze-dried and transferred to a porcelain boat. The samples were heated in a tube furnace at 5 °C min⁻¹ and kept 900 °C for 2 h to obtain Co/NC.

2.1.3. Synthesis of Co-NC

Acetic acid (0.6 mL), chitosan (0.6 g) and cobalt acetate tetrahydrate (199.2 mg) were dissolved in 20 mL deionized water, which was recorded as the solution A. Zinc acetate (3.668 g) was dissolved in 20 mL deionized water, which was recorded as the solution B. The solution A and solution B were uniformly mixed, the

formed mixture was freeze-dried and transferred to a porcelain boat. The samples were heated in a tube furnace at 5 °C min⁻¹ and kept 900 °C for 3 h to obtain Co-NC.

2.1.4. Synthesis of Co-NC-AD-0.5, Co-NC-AD-1, and Co-NC-AD-1.5

100 mg Co-NC and 10 mg, 20 mg and 30 mg CoCl₂ were added to 10 mL isopropanol, respectively, and the resulting mixture was ultrasonically dispersed for 2 h and then vigorously stirred for 12 h. After centrifugal cleaning and vacuum drying, the obtained product was transferred to a porcelain boat. The samples were heated in a tube furnace at 3 °C min⁻¹ and kept 900 °C for 3 h. The obtained products are labeled as Co-NC-AD-0.5, Co-NC-AD-1, and Co-NC-AD-1.5, respectively. The final Co-NC-AD-1 is represented as Co-NC-AD.

2.2. Characterization methods

X-ray diffraction (XRD) patterns were analyzed using a Rigaku D/max2600 X-ray diffractometer (equipped with Cu K_α radiation, $\lambda = 1.5418$ Å). Scanning electron microscopy (SEM, Hitachi S-8010) and transmission electron microscopy (TEM, JEM-2100F) were used to characterize the morphology and structure of the samples. Selected area electron diffraction (SAED) was also observed by JEM-2100F and energy-dispersive X-ray spectroscopy (EDS) was mounted to analyze the information of element distribution in the sample. X-ray photoelectron spectroscopy (XPS, ESCALAB-250) was performed using a K_α X-ray spectrometer (ThermoFisher Scientific Company) with an Al source, with a standard binding energy of 284.8 eV for C 1s. The inductively coupled plasma-optical emission spectroscopy (ICP-OES) was used to detect the metal content in the sample. The Brunauer-Emmett-Teller (BET) specific surface area and Barret-Joyner-Halenda (BJH) pore size distribution of the sample was analyzed using a gas adsorption analyzer. Soft X-ray emission spectrometer (SXES) were operated using X-ray spectrometer SS-94000SXES mounted on JSM-7900F, equipped at Electron Microscopy Center Jilin University. The graphitization degree (I_b/I_c) of the samples was measured by Raman spectroscopy using TESCAN S9000G, and the excitation wavelength is 514.5 nm. Electron energy loss spectroscopy (EELS) spectra (Gatan Inc., HV-GIF) mounted on TEM (Jeol Ltd., JEM ARM 1300S) for Co L₂, L₃ edges were recorded with an energy dispersion of 0.2 eV ch⁻¹.

2.3. X-ray absorption fine structure (XAFS) measurement and analysis method

The X-ray absorption spectra of Co K-edge were collected at 4B9A diffraction experimental station in Beijing Synchrotron Radiation Facility (BSFR). Experimental data was collected in fluorescence mode using the Lytle detector, and corresponding reference samples were collected in transmission mode. X-ray absorption near edge structure (XANES) data were normalized by the Athena module of Demeter software packages, and extended X-ray absorption fine structure (EXAFS) data were obtained by Fourier transform.

3. Results and discussion

3.1. Microstructure characterization

The synthesis step of Co-NC-AD catalyst with hierarchical porous structure is shown in Fig. 1(a). The simple synthesis method has good repeatability. The 4s and 4p electrons of Co²⁺ or Zn²⁺ can be used to coordinate the amino and carboxyl groups on chitosan through the competitive complexation to obtain hydrogel

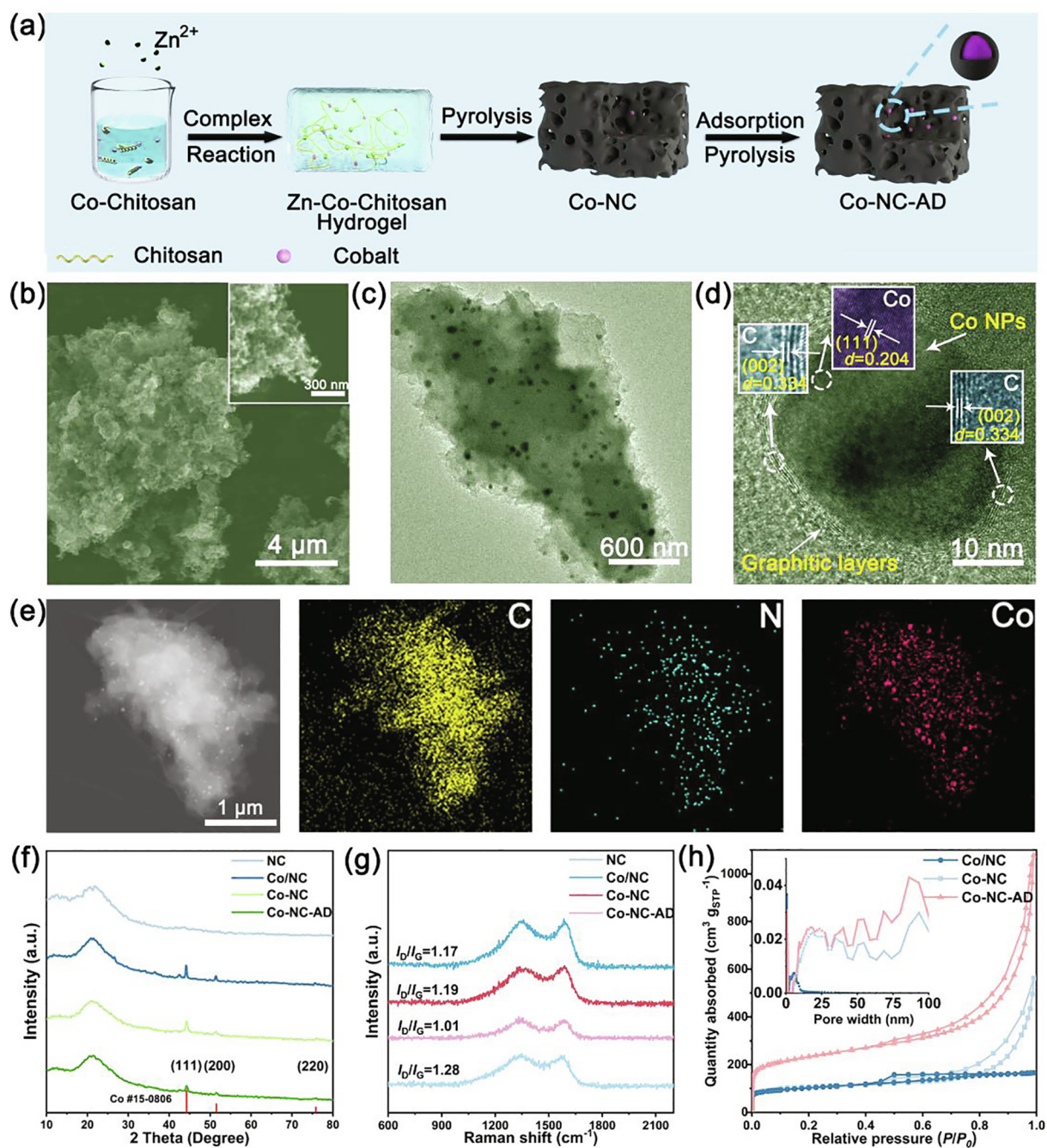


Fig. 1. (a) Schematic diagram of the preparation process of Co-NC-AD. (b) SEM, (c) TEM and (d) HRTEM images of Co-NC-AD. (e) STEM image and the corresponding elemental maps of Co-NC-AD. (f) X-ray diffraction patterns and (g) Raman spectra of NC, Co/NC, Co-NC and Co-NC-AD samples. (h) N_2 adsorption–desorption isotherms of Co/NC, Co-NC and Co-NC-AD samples, and the inset is the aperture distribution curve.

precursors in which Zn and Co are uniformly dispersed [41,42]. Co-NC was obtained after freeze-drying and high-temperature carbonization steps. In this process, the chitosan precursors were converted into nitrogen-doped carbon (NC), and the cobalt ions became the Co-NPs encapsulated by graphitic layers under the carbon reduction at high temperature. The optimized cobalt concentration and pyrolysis temperature were 0.04 M and 900 °C, respectively (Figs. S1 and S2). In order to further increase the number of Co-NPs, we adopted post-adsorption and secondary pyrolysis steps to obtain Co-NC-AD, and the optimized concentration of the adsorbed metal ions was 1 mg mL⁻¹ (Figs. S3–S6).

Scanning electron microscopy (SEM) image in Fig. 1(b) manifested that the Co-NC-AD catalyst appeared as a porous carbon structure, in which uniform Co-NPs (~25 nm) were loaded on the three-dimensional (3D) carbon framework. Compared with the Co-NC, the pore structure of Co/NC in Fig. S7 was significantly reduced. The introduction of zinc species has two main functions: (1) The zinc ions act as fences in the precursor, which minimizes the accumulation of cobalt species during the pyrolysis process, thereby facilitating the formation of uniform-sized Co-NPs. (2) Utilizing the low melting point and volatile characteristics of zinc species, they have a pore-forming effect during the high-temperature carbonization process, which is conducive to the for-

mation of hierarchically porous structures [43–45]. In order to increase the number of Co-NPs, the comparative samples (Co-NC-AD-0.5, Co-NC-AD-1.5, Co-NC-AD-1.0) with different metal adsorption concentrations were obtained through the post-adsorption strategy. The number of Co-NPs decreased when the metal adsorption concentration was too low. Whereas the non-uniform Co-NPs were formed when the metal adsorption concentration was too high. The aforementioned analysis was also confirmed by using transmission electron microscopy (TEM). In addition, the high-resolution TEM (HRTEM) identified that uniform Co-NPs were wrapped in graphitic layers with high curvature (Fig. 1d). The interplanar spacing of cobalt species was 0.204 nm, corresponding to the Co (111) crystal plane. The number of graphitic layers was around ~ 4 layers. The layer spacing of graphitic layers was 0.334 nm, i.e., the C (002) plane. More locations were randomly selected to scan, and the chainmail structure was found where Co-NPs were wrapped by some graphitic layers in the 3D carbon framework. The elemental mapping indicated that the Co-NC-AD catalyst contains C, N, O, and Co, in which the cobalt species existed in the form of NPs (Fig. 1e). ICP-OES confirmed that the content of cobalt species was 1.17 wt% (Table S1).

XRD in Fig. 1(f) revealed that there was a wide peak near 24.8° in Co-NC-AD and Co-NC corresponding to the C (002) plane. The diffraction peak at 44.2° , 51.5° and 71.8° corresponded to Co (111), (200) and (220) crystal plane [46,47]. The graphitization degree of carbon support was analyzed by Raman spectroscopy (Fig. 1g). Compared with Co-NC, Co-NC-AD uncovered a lower I_D/I_G value indicating a higher graphitization (a variety of concentrations were introduced in Table S2). The presence of M-NPs is beneficial to catalyze the formation of graphitic carbon structures at high temperature. The high graphitic carbon structure facilitates improving the overall conductivity of the catalyst and promote the electron transfer process [48]. The N_2 adsorption and desorption curve as shown in Fig. 1(h) indicated that the Co-NC-AD exhibited a higher BET specific surface area ($754.3 \text{ m}^2 \text{ g}^{-1}$) and an average pore diameter of 8.9 nm. It further identified the pore-forming effect of the zinc species. The pore size distribution curve uncovered that the Co-NC-AD held a hierarchical porous structure, which was of great significance to the improvement of catalytic performance. ORR mostly occurs at the three-phase interfaces. The hierarchical porous structure of the catalysts contributes to exposure of more three-phase interfaces, thereby improving the reaction kinetics. Micropores ($< 2 \text{ nm}$) can accommodate a large number of active sites; mesopores (2–50 nm) and macropores ($> 50 \text{ nm}$) facilitate the mass transfer process and increase the accessibility of reactants and active sites, thereby improving the overall catalytic efficiency [49].

3.2. Electronic structure analysis

High-resolution XPS analyzed the composition of the sample surface, which was composed of Co, C, N and O (Fig. S8). As shown in the Fig. 2(a), the N 1s spectrum of Co-NC-AD can be deconvoluted into four peaks, which were pyridine N (398.4 eV), pyrrole N (400.2 eV), graphite N (401.2 eV), and nitrogen N (403.5 eV) [50,51]. Compared with Co-NC, the graphite N increased from 22.26% to 39.49% and the Co-N increased from 13.03% to 24.20% in Co-NC-AD (Figs. S9 and S10, Table S3). It indicated that post-adsorption and secondary pyrolysis were beneficial to the graphitization of carbon support and the formation of more Co-N coordination structures. Studies have shown that high pyridine N content is beneficial to increase the onset potential for ORR and promote the four-electron transfer pathway, and high graphite N content helps to increase the limiting current density [52,53]. Both graphite and pyridine N species promote the adsorption and activation of oxygen molecules by generating partial positive charges

at adjacent carbon atoms. In Fig. 2(b), the Co 2p spectrum was divided into Co $2p_{1/2}$ and Co $2p_{3/2}$. Most cobalt species mainly existed divalently. Compared with Co-NC, the Co $2p_{3/2}$ peak position in Co-NC-AD had a right shift revealing the increase of the Co valence state [54,55]. The introduction of more Co-NPs in the post-adsorption process causes more Co-NPs to transfer electrons to the surrounding graphitic layers. As a newly used technique to identify elemental composition and chemical valence state, SXES has great potential in the field of energy research. We analyzed the electronic structure of carbon by using SXES. Compared with the NC (139.01 eV), the absorption peak positions of Co-NC-AD (139.25 eV) and Co-NC (139.12 eV) shifted right, indicating that the introduction of metallic cobalt species caused the change of electronic structure for graphitic layers (Fig. 2c) [56]. The larger shift of the absorption peak position in Co-NC-AD also confirmed that the additional metal cobalt species introduced in the post-adsorption process led to more activated graphitic layers. The electronic configuration of the activated graphitic layers is optimized and acts as the active sites, resulting in moderate adsorption strength with oxygen reduction intermediates and good catalytic activity [29,46].

XANES and EXAFS measurements were further used to study the electronic structure and geometric structure of the cobalt species in the catalyst. As seen from the XANES spectrum (Fig. 2d), the K-edge absorption edge of Co-NC-AD was located between CoO and Co_2O_3 , indicating that the Co valence state in Co-NC-AD was located between +2 and +3. Compared with Co-NC, the absorption-edge energy of Co-NC-AD moved towards the positive direction, indicating that the additional introduction of cobalt species during the post-adsorption step was beneficial to the increase of the Co valence state. The peaks at $780.6 \pm 0.2 \text{ eV}$ and $796.2 \pm 0.2 \text{ eV}$ in the EELS corresponded to the Co L_3 and L_2 edges, respectively (Fig. 2e). The smaller L_3/L_2 value of Co-NC-AD may prove that the valence state of Co species was higher than that of Co-NC. The above experimental results were in agreement with those obtained by XPS analysis [57]. The increase in the valence of the cobalt species manifested that the inner Co-NPs transfer more electrons to the outer graphite layers, thereby affecting the change of electron distribution in the outer graphitic layers. Moreover, synchrotron radiation combined with SXES jointly confirmed that the Co-NPs are conducive to the activation of the surrounding graphitic layers. In addition, the peaks of Co-NC-AD at 1.4 and 2.1 Å corresponded to Co-N and Co-Co coordination from Co K-edge Fourier-transform EXAFS (FT-EXAFS) spectrum, respectively (Fig. 2f and Fig. S12) [58]. The wavelet-transform EXAFS spectrum (WT-EXAFS) also confirmed the above conclusions (Fig. 2g–i). The above results manifest that the chainmail catalyst is mainly composed of Co-NPs wrapped in graphitic layers, in which electron transfer occurs between Co-NPs and graphitic layers. The high nitrogen content in chitosan introduces more nitrogen-containing species to the catalyst. The presence of pyridine N species is conducive to the formation of Co-N coordination structures and the activation of the graphitic shells, which is conducive to the improvement of ORR activity.

3.3. Electrochemical performance

The ORR activity of Co-NC-AD and control samples in saturated 0.1 M KOH was studied by the rotating disk electrode (RDE) test. Cyclic voltammetry (CV) test confirmed that Co-NC-AD had an obvious reduction peak at (0.75 V), proving its higher ORR activity (Fig. S13). The linear sweep voltammetry (LSV) test manifested that NC without cobalt doping showed the worst ORR activity, indicating that Co-NPs had a positive effect on ORR activity (Fig. 3a). The small reduction peak in the ORR polarization curve is due to the phenomenon of concentration polarization [59]. After

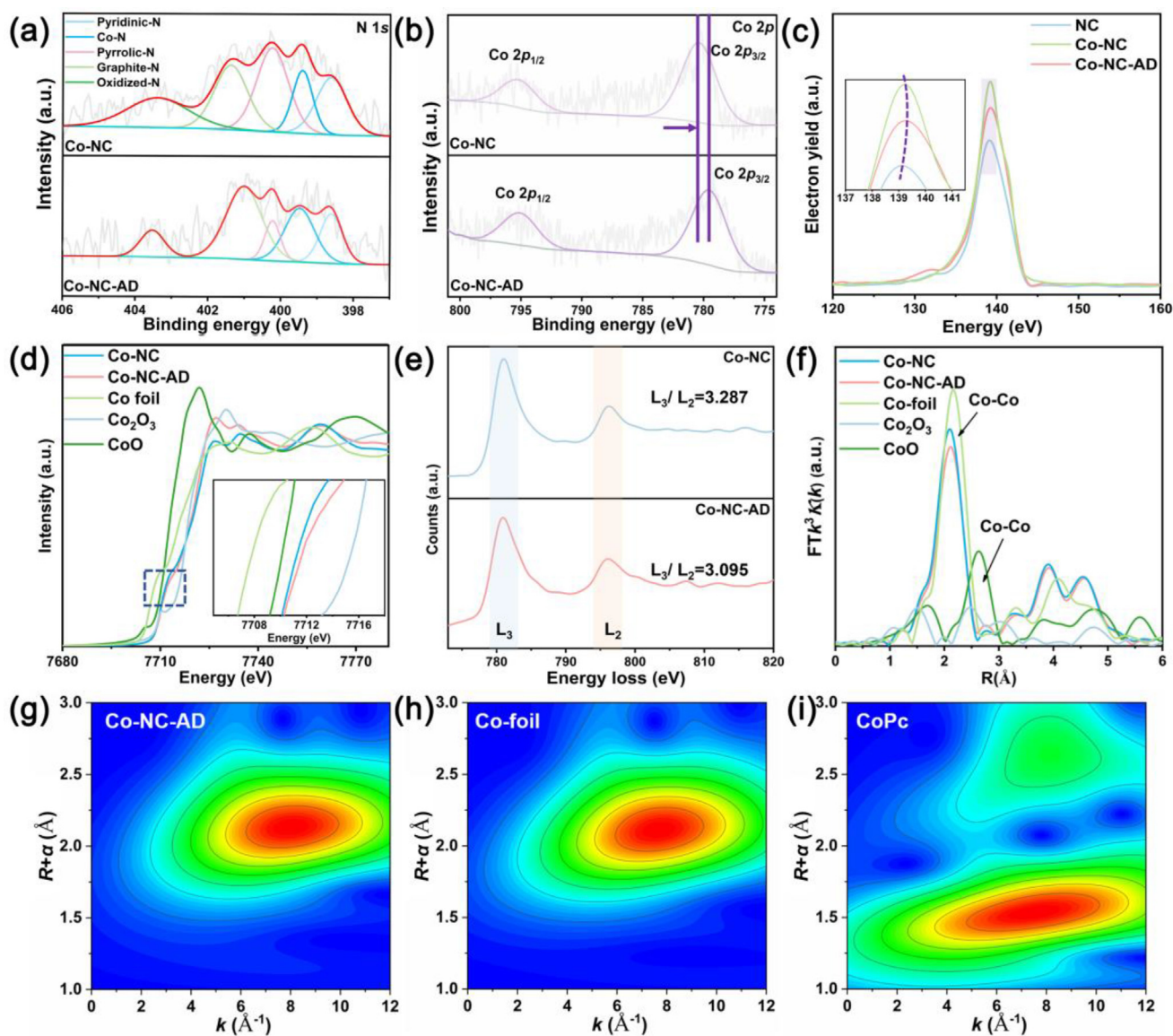


Fig. 2. Spectroscopy analysis. High-resolution XPS spectrum of (a) N 1s and (b) Co 2p for Co-NC and Co-NC-AD samples. (c) SXES spectra of Co-NC-AD and control sample. X-ray absorption profiles of the Co-NC-AD and control samples: (d) Co K-edge XANES spectra of Co-NC-AD and other control samples. (e) Electron energy loss spectrum (EELS) of Co L_3 and L_2 edges for Co-NC and Co-NC-AD. (f) Co K-edge Fourier-transform EXAFS spectra of Co-NC-AD and other control samples. Wavelet transform contour plots of Co K-edge at R space for (g) Co-NC-AD, (h) Co foil, and (i) CoPc.

regulating the doping number of cobalt species, Co-NC-AD confirmed the best ORR catalytic performance ($E_{\text{onset}} = 0.95$ V, $E_{1/2} = 0.86$ V), far exceeding the commercial Pt/C and most non-noble metal catalysts (Table S4). The introduction of zinc species in Co-NC-AD facilitates the formation of uniform-sized Co-NPs and hierarchical porous structure, greatly promoting the mass transfer process in the catalytic reaction. In order to verify the effect of the post-adsorption step, the ORR activity of the non-adsorbed sample (Co-NC) was compared with that of the samples with different adsorption concentrations (Co-NC-AD-0.5 and Co-NC-AD-1.5). The concentration of metal ions in the post-adsorption step was optimized to be 1 mg mL^{-1} (Figs. S14 and S15). When there was no adsorption or adsorption concentration was low, the number of Co-NPs formed was small, resulting in lower ORR activity. However, when the adsorption concentration was too high, it was not conducive to the formation of uniform Co-NPs. It can be seen from the SEM image that some Co-NPs were precipitated on the surface, which might be caused by the Oswald

ripening effect. The Co-NPs with high density and uniform size were conducive to the electron transfer process with the surrounding graphitic layers, so that the graphitic layers can be activated and the subsequent reaction process can proceed smoothly. As shown in Fig. 3(b), the LSV curves at different rotational speeds proved that the reaction process was a first-order reaction kinetic process controlled by diffusion. The resulting K-L plots were shown in the inset of Fig. 3(b), and the electron transfer calculated by the K-L equation was 3.9. It proved that the reaction process was the four-electron reaction process. The rotating ring electrode (RRDE) test in Fig. 3(c) also proved that the electron transfer number was 4 and the hydrogen peroxide yield was 5%. The lower Tafel slope of Co-NC-AD indicated reaction kinetics was superior (Fig. 3d, Fig. S16 and Table S5). Due to the complex working environment of fuel cells, the larger challenges are presented to the durability and stability of the catalyst. The accelerated durability test (ADT) showed that the $E_{1/2}$ and E_{onset} of Co-NC-AD did not obviously decrease after 10000 cycles of cycle stability test

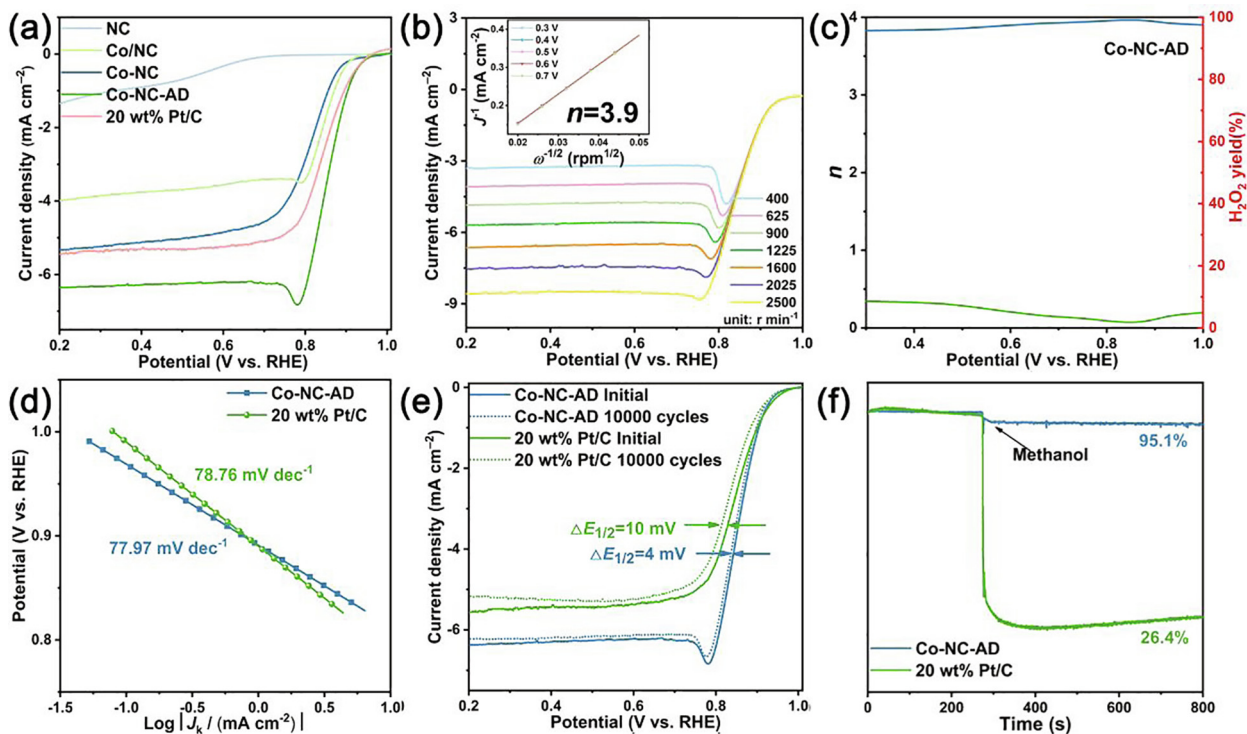


Fig. 3. Electrochemical performance. (a) The LSV curve of Co-NC-AD and control samples in O₂ saturated 0.1 M KOH. (b) LSV curves for Co-NC-AD at different rotating rates. (c) Electron transfer number and H₂O₂ yield for Co-NC-AD. (d) Tafel plots for Co-NC-AD and 20 wt% Pt/C. LSV curves of Co-NC-AD and 20 wt% Pt/C before and after 10,000 cycles CV in 0.1 M KOH. (f) Chronoamperometric curves of a methanol test with Co-NC-AD and 20 wt% Pt/C.

(Fig. 3e). The TEM image of the catalyst after the ADT test uncovered that the catalyst still maintained the original morphology without structural damage. In Co-NC-AD, Co-NPs were still surrounded by graphitic layers (Fig. S17). The anti-methanol poisoning experiment proved that Co-NC-AD had a good anti-methanol ability (Fig. 3f). In the interval of the non-Faraday potential range of 0.995–1.11 V, by linearly fitting the curves of different sweep speeds and current densities, the electric double layers (C_{dl}) capacitance value is 7.25 mF cm^{-2} (Fig. S18). This structure avoids the direct contact between the Co-NPs and electrolytes, which plays an important role in improving its stability and durability.

Excellent ORR performance is conducive to providing good discharge performance for zinc-air batteries, so Co-NC-AD was assembled into zinc-air battery to evaluate its practical application value (Fig. 4a). As shown in Fig. 4(b), the open-circuit voltage of the Co-NC-AD was 1.458 V, which was higher than that of 20 wt% Pt/C and most non-noble metal catalysts. The assembled a zinc-air battery can light up the light emitting diode (LED) light board with “JLU” subtitles, demonstrating its practical application in electronic equipment (the inset of Fig. 4c). In addition, the zinc-air battery based on the Co-NC-AD catalyst exhibited a discharge specific capacity of 808 mAh g_{Zn}^{-1} at 5 mA cm^{-2} , which was higher than the 718 mAh g_{Zn}^{-1} of Pt/C and most non-noble metal catalysts (Fig. 4c, Table S6). As shown in Fig. 4(d and e), the galvanostatic discharge curves under different current densities indicated that the zinc-air battery with Co-NC-AD held good rate capacity and stability. The discharge curve and power density (194 mW cm^{-2}) were shown in Fig. 4(f), exceeding the commercial Pt/C. In summary, Co-NC-AD showed superior discharge performance in zinc-air battery, which was related to the intrinsic ORR activity and structural characteristics of the catalyst. The unique hierarchical porous structure of Co-NC-AD can accommodate more active sites and greatly promote the catalytic mass transfer process, so it exhibits good performance in zinc-air batteries.

3.4. Exploration of electron shuttle based on DFT calculation

DFT calculation was used to further prove the influence of the electron shuttle effect between Co-NPs and the graphitic layers on the ORR activity. Based on the experimental results, we adopted Co-NPs wrapped in a single-walled graphitic shell as a model for the next discussion (Fig. 5a). In the NC model without Co, oxygen molecules cannot be adsorbed on surface carbon that acted as active sites. Compared with NC, the electron density of C as the active site in Co-NPs@NC was significantly higher, which meant that the inner Co-NPs transferred electrons to the outer graphitic layers (Fig. 5b) [60]. The electrons were then transferred to oxygen molecules through C–N bonding, contributing to the cleavage of the O–O bond. The partial densities of states (PDOS) for O-2p and C-1p in Fig. 5(c) further confirmed the interaction mode between oxygen molecules and active sites. The O-2p orbital resonated with the C-1p orbital at some peak positions, proving that hybridization between O-2p and C-1p orbital occurs [31]. This hybridization method facilitated the smooth adsorption process between the active sites and the oxygen molecules, thereby obtaining excellent ORR activity. The inner Co-NPs serve electron contributors to provide electrons to the outer graphitic layers, becoming the true source of catalytic activity [46]. In addition, the excellent stability of Co-NC-AD is derived from the protection of external C–N bindings, thereby avoiding the phase change of inner cobalt cores in contact with strong oxidizing or corrosive environments.

4. Conclusions

In conclusion, we utilized the cheap biomass material-chitosan as the precursor, using competitive complexation and post-absorption strategies to construct “chainmail catalysts” with graphitic layers encapsulated Co-NPs structure. The obtained Co-NC-AD catalyst had a high $E_{1/2}$ (0.86 V) and E_{onset} (0.95 V), which

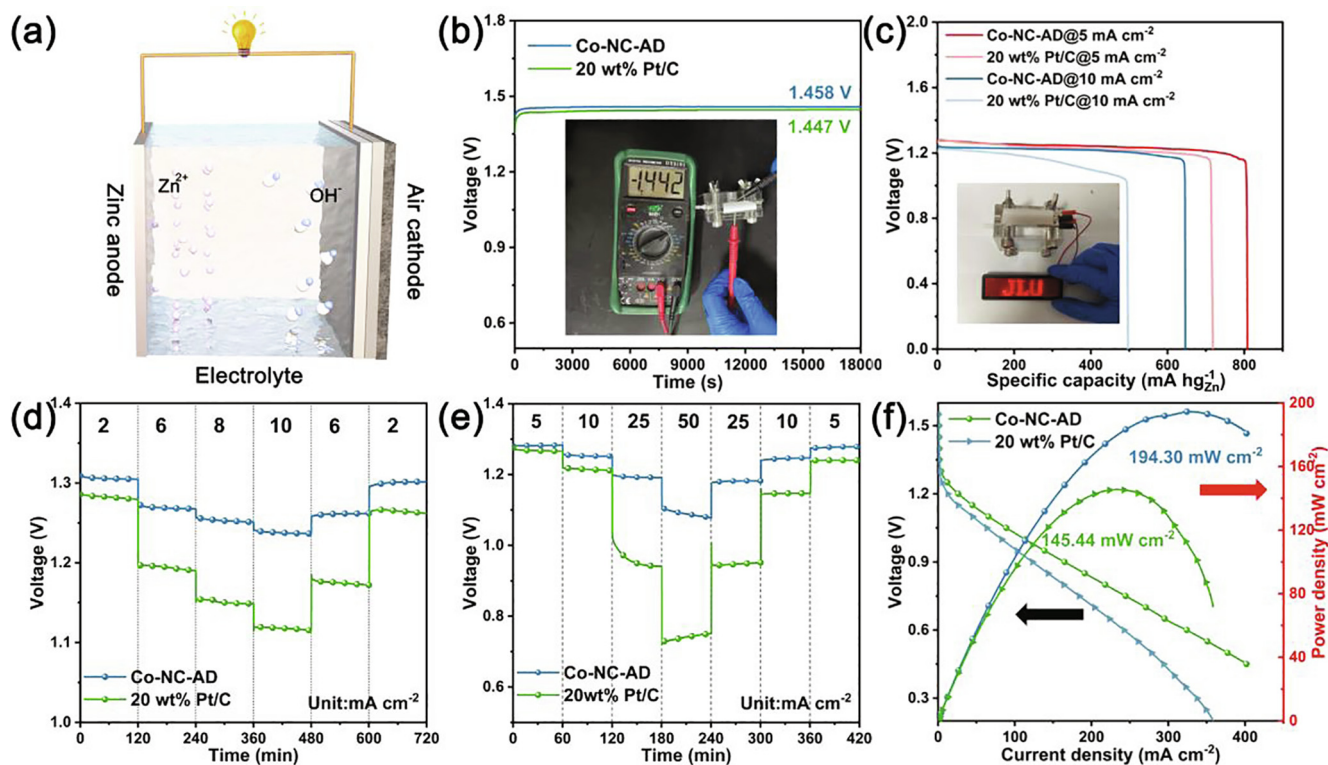


Fig. 4. Zinc-air battery performance. (a) Schematic diagram of the zinc-air battery. (b) Open-circuit voltage curves of the zinc-air battery using Co-NC-AD and 20 wt% Pt/C. And the inset digital photograph is open-circuit voltage. (c) Specific capacity at different current densities of Co-NC-AD and 20 wt% Pt/C, the inset diagram is LED panel lighting by Co-NC-AD. Galvanostatic discharge curves for zinc-air battery using Co-NC-AD and 20 wt% Pt/C at (d) low and (e) high current densities. (f) Discharge curves and power density of the Co-NC-AD and 20 wt% Pt/C.

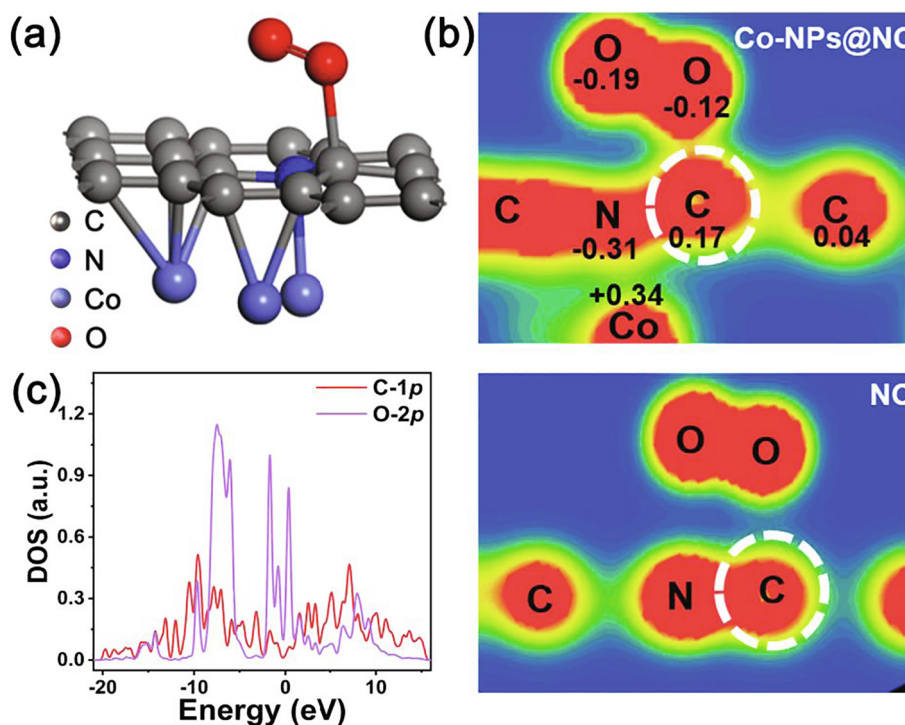


Fig. 5. (a) Model schematic diagram of CO-NC-AD catalyst, in which gray, dark blue, light blue and red spheres represent C, N, Co and O atoms respectively. (b) Charge density distribution of Co-NPs@NC and NC systems, where + and - represent gained and lost electrons respectively. (c) PDOS diagram of C-1p and O-2p for Co-NPs@NC system.

was superior to the commercial Pt/C and most non-noble metal catalysts. The addition of Zn species is beneficial to the formation

of hierarchically porous structures and uniform Co-NPs. Spectrum analysis combined with DFT calculation jointly confirmed the exist-

tence of Co-NPs regulated the electron configuration of the graphitic layers, via the electron shuttle effect in the graphitic layers to facilitate the adsorption behavior between oxygen molecules and active sites. In addition, the encapsulation effect of the graphitic layers effectively avoids the direct contact between the graphitic layers and Co-NPs, which is beneficial to improve the stability and the ability to resist methanol poisoning. The zinc-air battery assembled with Co-NC-AD as the cathode catalyst has a higher specific capacity and open-circuit voltage than the commercial Pt/C, revealing its potential value in practical applications. Our biomass-derived chainmail structure of the carbon shells wrapped M-NPs provides a new route for the design of electrocatalysts with high activity and high stability.

Declaration of competing interest

The authors declare that they have no known competing financial interests or personal relationships that could have appeared to influence the work reported in this paper.

Acknowledgments

This research is supported by the National Natural Science Foundation of China (51872115, 51932003), the 2020 International Cooperation Project of the Department of Science and Technology of Jilin Province (20200801001GH), the Project supported by State Key Laboratory of Luminescence and Applications (KLA-2020-05), the Project for Self-innovation Capability Construction of Jilin Province Development and Reform Commission (2021C026). The Beijing Synchrotron Radiation Facility (BSRF) is greatly acknowledged for providing us the beam time on beamlines 4B9A for the XAFS measurements.

Appendix A. Supplementary data

Supplementary data to this article can be found online at <https://doi.org/10.1016/j.jechem.2022.01.047>.

References

- [1] X. Tian, X. Zhao, Y.Q. Su, L. Wang, H. Wang, D. Dang, B. Chi, H. Liu, J.M. Hensen Emiel, W. Lou Xiong, Y. Xia Bao, *Science* 366 (2019) 850–856.
- [2] J. Zhu, A.O. Elnabawy, Z. Lyu, M. Xie, E.A. Murray, Z. Chen, W. Jin, M. Mavrikakis, Y. Xia, *Mater. Today* 35 (2019) 69–77.
- [3] M. Zhou, H. Wang, M. Vara, Z.D. Hood, M. Luo, T.-H. Yang, S. Bao, M. Chi, P. Xiao, Y. Zhang, Y. Xia, *J. Am. Chem. Soc.* 138 (2016) 12263–12270.
- [4] Z. Xiang, A. Tan, Z. Fu, J. Piao, Z. Liang, *J. Energy Chem.* 49 (2020) 323–326.
- [5] J. Gan, J. Zhang, B. Zhang, W. Chen, D. Niu, Y. Qin, X. Duan, X. Zhou, *J. Energy Chem.* 45 (2020) 59–66.
- [6] H. Yuan, Q. Zhang, *J. Energy Chem.* 48 (2020) 107–108.
- [7] S.S. Sekhon, J. Lee, J. Park, *J. Energy Chem.* 65 (2022) 149–172.
- [8] C. Zhao, J. Liu, J. Wang, D. Ren, J. Yu, X. Chen, B. Li, Q. Zhang, *Adv. Mater.* 33 (2021) 2008606.
- [9] J. Wang, C. Zhao, J. Liu, D. Ren, B. Li, J. Huang, Q. Zhang, *Nano Mater. Sci.* 3 (2021) 313–318.
- [10] H. Wang, C. Weng, Z. Yuan, *J. Energy Chem.* 56 (2021) 470–485.
- [11] J. Gao, Y. Wang, H. Wu, X. Liu, L. Wang, Q. Yu, A. Li, H. Wang, C. Song, Z. Gao, M. Peng, M. Zhang, N. Ma, J. Wang, W. Zhou, G. Wang, Z. Yin, D. Ma, *Angew. Chem. Int. Ed.* 58 (2019) 15089–15097.
- [12] C. Xiao, X. Chen, Z. Fan, J. Liang, B. Zhang, S. Ding, *Nanotechnology* 27 (2016) 445402.
- [13] C. Zhang, W. Zhang, S. Yu, D. Wang, W. Zhang, W. Zheng, M. Wen, H. Tian, K. Huang, S. Feng, J.J. Bentzen, *ChemElectroChem* 4 (2017) 1269–1273.
- [14] Z. Sheng, L. Shao, J. Chen, W. Bao, F. Wang, X. Xia, *ACS Nano* 5 (2011) 4350–4358.
- [15] H. Fei, J. Dong, M.J. Arellano-Jiménez, G. Ye, N. Dong Kim, E.L.G. Samuel, Z. Peng, Z. Zhu, F. Qin, J. Bao, M.J. Yacamán, P.M. Ajayan, D. Chen, J.M. Tour, *Nat. Commun.* 6 (2015) 8668.
- [16] H.N. Fernandez-Escamilla, J. Guerrero-Sanchez, E. Contreras, J.M. Ruiz-Mariscal, G. Alonso-Nunez, O.E. Contreras, R.M. Felix-Navarro, J.M. Romo-Herrera, N. Takeuchi, *Adv. Energy Mater.* 11 (2021) 2002459.
- [17] S. Yang, L. Zhi, K. Tang, X. Feng, J. Maier, K. Müllen, *Adv. Funct. Mater.* 22 (2012) 3634–3640.
- [18] G. Tian, Q. Zhang, B. Zhang, Y. Jin, J. Huang, D. Su, F. Wei, *Adv. Funct. Mater.* 24 (2014) 5956–5961.
- [19] Y. Zhao, J. Wan, H. Yao, L. Zhang, K. Lin, L. Wang, N. Yang, D. Liu, L. Song, J. Zhu, L. Gu, L. Liu, H. Zhao, Y. Li, D. Wang, *Nat. Chem.* 10 (2018) 924–931.
- [20] Y. Qiao, F. Kong, C. Zhang, R. Li, A. Kong, Y. Shan, *Electrochim. Acta* 339 (2020) 135923.
- [21] X. Zhou, X. Liu, J. Zhang, C. Zhang, S.J. Yoo, J.G. Kim, X. Chu, C. Song, P. Wang, Z. Zhao, D. Li, W. Zhang, W. Zheng, *Carbon* 166 (2020) 284–290.
- [22] H. Zhao, T. Xing, L. Li, X. Geng, K. Guo, C. Sun, W. Zhou, H. Yang, R. Song, B. An, *Int. J. Hydrog. Energy* 44 (2019) 25180–25187.
- [23] K. Song, Y. Feng, W. Zhang, W. Zheng, *J. Energy Chem.* 67 (2022) 391–422.
- [24] W. Yan, Y. Wu, Y. Chen, Q. Liu, K. Wang, N. Cao, F. Dai, X. Li, J. Jiang, *J. Energy Chem.* 44 (2020) 121–130.
- [25] W. Liu, D. Rao, J. Bao, L. Xu, Y. Lei, H. Li, *J. Energy Chem.* 57 (2021) 428–435.
- [26] L. Zhang, J. Xiao, H. Wang, M. Shao, *ACS Catal.* 7 (2017) 7855–7865.
- [27] F. Yang, D. Deng, X. Pan, Q. Fu, X. Bao, *Natl. Sci. Rev.* 2 (2015) 183–201.
- [28] H. Khani, N.S. Grundish, D.O. Wipf, J.B. Goodenough, *Adv. Energy Mater.* 10 (2020) 1903215.
- [29] X. Cui, P. Ren, D. Deng, J. Deng, X. Bao, *Energy Environ. Sci.* 9 (2016) 123–129.
- [30] J. Deng, P. Ren, D. Deng, X. Bao, *Angew. Chem. Int. Ed.* 54 (2015) 2100–2104.
- [31] D. Deng, L. Yu, X. Chen, G. Wang, L. Jin, X. Pan, J. Deng, G. Sun, X. Bao, *Angew. Chem. Int. Ed.* 52 (2013) 371–375.
- [32] J. Deng, P. Ren, D. Deng, L. Yu, F. Yang, X. Bao, *Energy Environ. Sci.* 7 (2014) 1919–1923.
- [33] X. Chen, J. Xiao, J. Wang, D. Deng, Y. Hu, J. Zhou, L. Yu, T. Heine, X. Pan, X. Bao, *Chem. Sci.* 6 (2015) 3262–3267.
- [34] F. Guinea, *Phy. Rev. B* 75 (2007) 235433.
- [35] X. Chen, S. Huang, H. Zhang, *J. Alloys Compd.* 894 (2022) 162508.
- [36] X. Chen, H. Zhang, N. Lai, *J. Mater. Sci.* 55 (2020) 11382–11390.
- [37] X. Lv, W. Xu, W. Tian, H. Wang, Z. Yuan, *Small* (2021) 2101856.
- [38] L. Yu, D. Deng, X. Bao, *Angew. Chem. Int. Ed.* 59 (2020) 15294–15297.
- [39] B. Huang, Y. Liu, Z. Xie, *J. Energy Chem.* 54 (2021) 795–814.
- [40] B. Huang, M. Xia, J. Qiu, Z. Xie, *ChemNanoMat* 5 (2019) 682–689.
- [41] Z. Lu, B. Wang, Y. Hu, W. Liu, Y. Zhao, R. Yang, Z. Li, J. Luo, B. Chi, Z. Jiang, M. Li, S. Mu, S. Liao, J. Zhang, X. Sun, *Angew. Chem. Int. Ed.* 58 (2019) 2622–2626.
- [42] D. Liu, B. Wang, H. Li, S. Huang, M. Liu, J. Wang, Q. Wang, J. Zhang, Y. Zhao, *Nano Energy* 58 (2019) 277–283.
- [43] Y. Chen, S. Ji, Y. Wang, J. Dong, W. Chen, Z. Li, R. Shen, L. Zheng, Z. Zhuang, D. Wang, Y. Li, *Angew. Chem. Int. Ed.* 56 (2017) 6937–6941.
- [44] P. Yin, T. Yao, Y. Wu, L. Zheng, Y. Lin, W. Liu, H. Ju, J. Zhu, X. Hong, Z. Deng, G. Zhou, S. Wei, Y. Li, *Angew. Chem. Int. Ed.* 55 (2016) 10800–10805.
- [45] X. Hai, X. Zhao, N. Guo, C. Yao, C. Chen, W. Liu, Y. Du, H. Yan, J. Li, Z. Chen, X. Li, Z. Li, H. Xu, P. Lyu, J. Zhang, M. Lin, C. Su, S.J. Pennycook, C. Zhang, S. Xi, J. Lu, *ACS Catal.* 10 (2020) 5862–5870.
- [46] H. Zhang, T. Wang, J. Wang, H. Liu, T.D. Dao, M. Li, G. Liu, X. Meng, K. Chang, L. Shi, T. Nagao, J. Ye, *Adv. Mater.* 28 (2016) 3703–3710.
- [47] X. Lv, Z. Xiao, H. Wang, X. Wang, L. Shan, F. Wang, C. Wei, X. Tang, Y. Chen, *J. Energy Chem.* 54 (2021) 626–638.
- [48] J. Ren, Y. Wang, L. Chen, L. Gao, W.W. Tian, Z. Yuan, *Chem. Eng. J.* 389 (2020) 124408.
- [49] L. Gao, M. Xiao, Z. Jin, C. Liu, J. Ge, W. Xing, *J. Energy Chem.* 35 (2019) 17–23.
- [50] X. Fu, P. Zamani, J.-Y. Choi, F.M. Hassan, G. Jiang, D.C. Higgins, Y. Zhang, M.A. Hoque, Z. Chen, *Adv. Mater.* 29 (2017) 1604456.
- [51] X. Jiang, J. Chen, F. Lyu, C. Cheng, Q. Zhang, X. Wang, A. Mahsud, L. Zhang, Q. Zhang, *J. Energy Chem.* 59 (2021) 482–491.
- [52] X. Ge, A. Sumboja, D. Wu, T. An, B. Li, F.W.T. Goh, T.S.A. Hor, Y. Zong, Z. Liu, *ACS Catal.* 5 (2015) 4643–4667.
- [53] M.I. Awad, T. Ohsaka, *J. Power Sources* 226 (2013) 306–312.
- [54] T. Lukaszczk, K. Flechtner, L.R. Merte, N. Jux, F. Maier, J.M. Gottfried, H.-P. Steinrück, *J. Phys. Chem. C* 111 (2007) 3090–3098.
- [55] G. Zhang, C. Huang, X. Wang, *Small* 11 (2015) 1215–1221.
- [56] T. Qin, W. Zhang, Y. Ma, W. Zhang, T. Dong, X. Chu, T. Li, Z. Wang, N. Yue, H. Liu, L. Zheng, X. Fan, X. Lang, Q. Jiang, W. Zheng, *Energy Stor. Mater.* 45 (2022) 33–39.
- [57] A.C. Foucher, N. Marcella, J.D. Lee, D.J. Rosen, R. Tapper, C.B. Murray, A.I. Frenkel, E.A. Stach, *ACS Nano* 15 (2021) 20619–20632.
- [58] T. Shen, X. Huang, S. Xi, W. Li, S. Sun, Y. Hou, *J. Energy Chem.* 68 (2021) 184–194.
- [59] Q. Wang, Z. Zhou, Y. Lai, Y. You, J. Liu, X. Wu, E. Terefe, C. Chen, L. Song, M. Rauf, N. Tian, S. Sun, *J. Am. Chem. Soc.* 136 (2014) 10882–10885.
- [60] X. Yang, D. Zhao, *Appl. Surf. Sci.* 544 (2021) 148765.